Mapping Bulk Electrical Properties with Non-Contact RF Measurements

by

Benjamin M. Schwartz

Submitted to the Department of Physics
in partial fulfillment of the requirements for the degree of

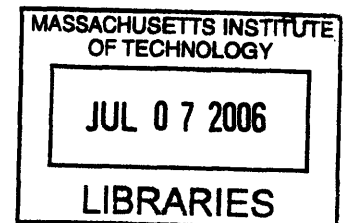Bachelor of Science in Physics with Electrical Engineering

at the

MASSACHUSETTS INSTITUTE OF TECHNOLOGY

[June 2006]
May 2006

Author . . . .
Department of Physics
May 19, 2006

Certified by . . . .
Professor Daniel Sodickson
Assistant Professor of Health Sciences and Technology
Thesis Supervisor

Accepted by . . . .
Professor David E. Pritchard
Senior Thesis Coordinator, Department of Physics

Mapping Bulk Electrical Properties with Non-Contact RF Measurements

by

Benjamin M. Schwartz

Submitted to the Department of Physics
on May 19, 2006, in partial fulfillment of the
requirements for the degree of
Bachelor of Science in Physics with Electrical Engineering

Abstract

The human body is composed primarily of dielectric tissue with spatially varying permittivity and conductivity. Traditional MRI does not measure these properties. Instead, the conductivity of the patient is a nuisance, causing unpredictable detuning of coils and field inhomogeneities. This thesis presents a method for mapping the electrodynamic properties of the patient's body with both MR and non-MR techniques. Such mapping has direct applications for medical imaging and SAR calculation.

Thesis Supervisor: Professor Daniel Sodickson
Title: Assistant Professor of Health Sciences and Technology

Acknowledgments

I owe a great deal to all the members of the Laboratory for Biomedical Imaging Research, but particularly to Daniel Sodickson and Aaron Grant. These two taught me the foundations necessary to tackle this problem, advised me on the best approaches at every stage, and showed me what it means to do academic research. They always made time for me to ask questions, and were always willing to consider a new idea, however outlandish. This thesis would have been inconceivable without their tremendous help.

Contents

List of Figures

List of Tables

12

Chapter 1

Background

1.1 Introduction

MRI coil designers commonly attempt to maximize the SNR of images acquired with their coils. The SNR of a coil depends strongly on its sensitivity, and a coil's sensitivity is determined by the strength of its magnetic field at each location. A human body, as a conductive object, distorts these fields, so coil designers must model the patient as part of the design process.

The effect of the patient on the coil's sensitivity becomes more noticeable in high-field imagng, as this effect grows with increasing field strength. At very high fields, nonuniformity in the sensitivity of the coils results in seriously detrimental distortion of the image. Not only does the nonuniformity of the sensitivity grow with increasing field strength, the strength of the dependence of the nonuniformity on the underlying permittivity and conductivity also increases. High-field imaging also suffers from an increase in SAR due to the B_1 fields, so detailed knowledge of the fields is important for patient safety.

The different effect of each patient on the MRI imaging coils is well known in clinical MRI, and has traditionally been seen as a nuisance. However, the strong sensitivity of high-field imaging to this inter-patient variation raises a question: can this variation be seen as data, rather than as noise?

1.2 A New Technique

The effect of the patient on the unloaded coil is often described as "detuning," meaning that the patient alters the coil's resonance structure. Resonances are directly measurable as peaks in the impedance of each coil at the resonant frequency. In a system with many coils, each coil is most sensitive to changes in a corresponding small region of space. The many measurements from different coils collectively form a spatial map of the electrical properties of the patient. Accordingly, this approach is tentatively named Radio-Frequency Impedance Mapping, or RFIM. RFIM makes no use of MR effects, so an RFIM device would not need a static field or gradient coils. At the start of this research, Aaron Grant and others in the Laboratory for Biomedical Imaging Research had already been investigating RFIM for several years [1].

1.3 Direct RFIM

1.3.1 Method

Direct RFIM is the simplest form of RFIM. A typical Direct RFIM device would consist of a large number of small coils held in fixed relative positions around the exterior of the patient. All the coils have nearly identical resonant frequencies. This description is based on a manuscript by Aaron Grant and Daniel Sodickson [2].

To acquire an image, the device tests the cross-impedance of every pair of coils at a frequency ω close to the resonances of all the coils. Consider a system with N coils indexed by i, j from 1 to N. Then the complex cross-impedance between two coils i and j is given by the integral over volume

$$Z_{ij} = \int_V \vec{\mathscr{E}}_i \cdot \vec{\mathscr{J}}_j d^3v$$

where $\vec{\mathscr{E}}_i$ is the electric field produced by the i'th coil and $\vec{\mathscr{J}}_j$ is the current density produced by the j'th coil. This formula neglects radiation to infinity, which is

presumed to be small compared to the interaction with nearby objects. Note that all of these quantities are complex. For consistency, complex quantities representing the magnitude and phase of oscillations occurring at frequency ω will appear in MATHSCR typeface throughout, e.g. $\mathscr{E}, \mathscr{M}$.

The currents induced by this impedance measurement should be small enough that the tissue of the patient may be viewed as having linear conductivity and permittivity. The further approximation that these quantities are isotropic allows us to rewrite the preceding equation as

$$Z_{ij} = \int_V \vec{\mathscr{E}_i} \cdot \left((\sigma + i\omega\epsilon) \vec{\mathscr{E}_j} \right) d^3v \tag{1.1}$$

$$= \int_V (\sigma + i\omega\epsilon) \vec{\mathscr{E}_i} \cdot \vec{\mathscr{E}_j} d^3v \tag{1.2}$$

where σ is the conductivity and ϵ is the permittivity. The purpose of RFIM is to map the values of these two parameters.

To convert the measurements of Z_{ij} into a spatial map of ϵ and σ, laboratory implementations of Direct RFIM employ an iterated electrodynamic simulation. In particular, a finite-difference time-domain (FDTD) simulation of the entire system is used to determine the $\vec{\mathscr{E}}$-fields that would be produced by each coil in the presence of some initial ϵ, σ map. The above integral is evaluated numerically to determine the Z for this map. A Levenberg–Marquardt optimizer is then applied to the (ϵ, σ) map. The optimizer changes the map until the simulated Z matches the measured Z.

1.3.2 Difficulties

The reconstruction of Direct RFIM images requires a tremendous amount of computation. Hardware that can reconstruct high-resolution 32-channel parallel-imaging MRI data in seconds takes days to reconstruct low-resolution RFIM using the method described here. The computation time is almost entirely in the FDTD simulation, which must be reevaluated with every iteration of the optimizer [3].

Direct RFIM is also difficult to consider analytically. The reconstruction process

is highly nonlinear, so its noise characteristics and stability are poorly understood.

1.4 MRI and RFIM

This thesis is concerned with extensions to the RFIM concept incorporating MRI technologies. Section 2.1 describes the potential for MRI to accelerate and stabilize the RFIM reconstruction process by providing additional information about the $\mathscr{E}$-fields. Section 2.2 describes a method by which MRI may improve the quality of RFIM images by determining where edges are likely to appear in the (ϵ, σ) map. Section 2.3 describes a technique to extract the property map directly from MRI data, without any impedance measurements at all.

Chapter 2

MRI-Assisted RFIM

If RFIM is implemented inside an MRI machine, MRI images may be used to improve the RFIM technique. In particular, MRI may provide extra information about image structure, accelerate image reconstruction, and even add more data to the map. Equipped with these three additional components, RFIM is referred to as MRI-assisted RFIM.

RFIM is highly compatible with MRI. RFIM requires only a set of resonant coils, much like the imaging coils commonly used in MRI. RFIM is not likely to be affected by the presence of a strong static field, as the Hall effect and similar static-field effects are not significant at MRI field strengths. If the RFIM resonant frequency is chosen to be the Larmor frequency, then the only additional requirements for RFIM-capable MRI are the ability to transmit with the surface coils and appropriate hardware for measuring their cross-impedances.

2.1 Linear RFIM

Overview

One approach to accelerating RFIM reconstruction is to linearize the problem. Specifically, consider the expression

$$Z_{ij} = \int_V \left(\sigma + i\omega\epsilon \right) \vec{\mathcal{E}}_i \cdot \vec{\mathcal{E}}_j d^3 v. \tag{2.1}$$

Consider ij as a single index, so that Z is a length-N^2 column vector. Let $\mathscr{F}$ be a N^2-by-∞ matrix containing the "field overlap" information, defined by

$$\mathscr{F}_{ij,\vec{x}} = \vec{\mathcal{E}}_i(\vec{x}) \cdot \vec{\mathcal{E}}_j(\vec{x}). \tag{2.2}$$

Finally, let ς be an ∞-by-1 column vector defined by

$$\varsigma_{\vec{x}} = \sigma(\vec{x}) + i\omega\epsilon(\vec{x}). \tag{2.3}$$

Then we may represent the integral above as the continuous matrix inner product

$$Z = \mathscr{F}\varsigma. \tag{2.4}$$

In this formulation, the goal of RFIM is to extract ς. If $\mathscr{F}$ is known, then determining ς is reduced to the relatively simple matter of solving a linear matrix equation. While not computationally trivial, this linear reconstruction would require far less computational effort than the iterative nonlinear approach required without knowledge of $\mathscr{F}$, the field overlap matrix.

2.1.1 Field Mapping

Magnetic Resonance Imaging can be used to accelerate RFIM by providing the field maps to calculate $\mathscr{F}$. $\mathscr{F}$ is determined by the electric fields generated by the coils. Conceptually, MRI is capable of measuring the harmonic magnetic field $\vec{\mathscr{B}}$. In a

harmonic field, $\nabla \times \vec{\mathcal{E}} = -i\omega\vec{\mathcal{B}}$. Therefore knowledge of $\vec{\mathcal{B}}$ is sufficient to reconstruct $\vec{\mathcal{E}}$ up to a potential field $\vec{\nabla}\phi$. This field is expected to be negligible, as it corresponds to the local deviation of the body from charge neutrality. Such deviation is strongly suppressed by the conductivity of tissue.

The details of MRI field mapping are slightly more complicated and preclude true linearization of the type described so far. To understand this process, ignore the problems of gradients and localization. Instead, consider a very small sample placed in the bore of the imager. This sample must be small enough that all fields are approximately uniform throughout its volume. Take the following definitions, as given by Hoult in [5]:

Table 2.1: Variable definitions for field mapping, following Hoult

Variable	Definition
I	the current applied to the transmitting coil
$\vec{B}_a$	the magnetic field generated by coil a at the sample location when a current I is applied
B_{ax}	the component of $\vec{B}_a$ in the x direction
ξ_{rs}	the complex harmonic voltage induced in coil s when coil r transmits
ω	the angular Larmor frequency
M	the sample magnetization
γ	the gyromagnetic ratio of the nuclei in question

Since the nuclear interactions are largely rotational about the z-axis (defined parallel to the $\vec{B}_0$ field), it is useful to define positively and negatively circularly polarized coordinate systems rotating about this axis at the Larmor frequency. As a notational device, for each harmonic field $\vec{\mathcal{Q}}$ let $\widetilde{\mathcal{Q}}^{\pm}$ be the $\pm$-circularly polarized complex harmonic component of $\mathcal{Q}$. From Hoult's Equations 14 and 15,

$$\widetilde{\mathcal{Q}}^{+} = \frac{\mathcal{Q}_x + i\mathcal{Q}_y}{2}; \tag{2.5}$$

$$\widetilde{\mathcal{Q}}^{-} = \frac{(\mathcal{Q}_x - i\mathcal{Q}_y)^*}{2}. \tag{2.6}$$

From Hoult's Equation 27,

$$\xi_{ab} = \omega\widetilde{\mathcal{M}}^{+}\frac{1}{\mathcal{I}_a}\left(\mathcal{B}_{bx} - i\mathcal{B}_{by}\right). \tag{2.7}$$

Suppose the magnetization was at equilibrium, but has just been subjected to a uniform pulse of length τ from coil a. Let M_0 be the equilibrium magnetization, and ignore magnetization decay. Then

$$\xi_{ab}(\tau) = \omega M_0 \sin\left(\gamma\tau\left|\widetilde{\mathscr{B}}_a^+\right|\right) \frac{-i\widetilde{\mathscr{B}}_a^+}{\left|\widetilde{\mathscr{B}}_a^+\right|} \frac{1}{\mathscr{I}_a} \left(\mathscr{B}_{bx} - i\mathscr{B}_{by}\right). \tag{2.8}$$

By the previous definitions,

$$\widetilde{\mathscr{B}}_b^- = \frac{\left(\mathscr{B}_{bx} - i\mathscr{B}_{by}\right)^*}{2}; \tag{2.9}$$

$$\xi_{ab}(\tau) = \frac{-2i\omega M_0}{\mathscr{I}_a} \sin\left(\gamma\tau\left|\widetilde{\mathscr{B}}_a^+\right|\right) \frac{\widetilde{\mathscr{B}}_a^+}{\left|\widetilde{\mathscr{B}}_a^+\right|} \widetilde{\mathscr{B}}_b^{-*}. \tag{2.10}$$

In Equation 2.10, M_0 is unknown, so the fields cannot be pulled out directly. However, we may cancel M_0:

$$\frac{\xi_{ab}(2\tau)}{\xi_{ab}(\tau)} = \frac{\sin\left(2\gamma\tau\left|\widetilde{\mathscr{B}}_a^+\right|\right)}{\sin\left(\gamma\tau\left|\widetilde{\mathscr{B}}_a^+\right|\right)} = 2\cos\left(\gamma\tau\left|\widetilde{\mathscr{B}}_a^+\right|\right); \tag{2.11}$$

$$\left|\widetilde{\mathscr{B}}_a^+\right| = \frac{1}{\gamma\tau} \arccos\left(\frac{\xi_{ab}(2\tau)}{2\xi_{ab}(\tau)}\right). \tag{2.12}$$

Equation (2.12) is the basis for standard B_1 mapping in MRI.

Although the magnitude of the field is of primary interest for MRI, other properties are useful in RFIM. In particular, if coil a is the only coil that can transmit, three other independent quantities are available from ξ. The first quantity is the ratio of the magnitudes of the negative circularly polarized field amplitudes:

$$\left|\frac{\xi_{ab}(\tau)}{\xi_{aa}(\tau)}\right| = \left|\frac{\widetilde{\mathscr{B}}_b^{-*}}{\widetilde{\mathscr{B}}_a^{-*}}\right| = \frac{\left|\widetilde{\mathscr{B}}_b^-\right|}{\left|\widetilde{\mathscr{B}}_a^-\right|}. \tag{2.13}$$

The other available quantities are relative phases. Let $u(x) \equiv x/|x|$. Take the phase

of $\mathscr{I}_a$ to be zero. Then

$$u\left(i\xi_{ab}(\tau)\right) = u\left(\widetilde{\mathscr{B}}_a^+\right) u\left(\widetilde{\mathscr{B}}_b^{-*}\right) = \frac{u\left(\widetilde{\mathscr{B}}_a^+\right)}{u\left(\widetilde{\mathscr{B}}_b^-\right)}; \qquad (2.14)$$

$$u\left(i\xi_{aa}(\tau)\right) = u\left(\widetilde{\mathscr{B}}_a^+\right) u\left(\widetilde{\mathscr{B}}_a^{-*}\right) = \frac{u\left(\widetilde{\mathscr{B}}_a^+\right)}{u\left(\widetilde{\mathscr{B}}_a^-\right)}. \qquad (2.15)$$

If it is possible to transmit with a coil b, then symmetrically we may additionally find $\left|\widetilde{\mathscr{B}}_b^+\right|$ and $u\left(\widetilde{\mathscr{B}}_b^+\right)/u\left(\widetilde{\mathscr{B}}_a^-\right)$. Note that it is not possible to determine $\left|\widetilde{\mathscr{B}}_a^-\right|$ or the absolute phase of any field. If these two quantities were known, they would be sufficient to reconstruct $\mathscr{B}_x$ and $\mathscr{B}_y$ for both coils. Since magnetic fields are divergence-free, the x and y components are sufficient to find $\vec{\mathscr{B}}$.

By letting a and b range over all the pairs of coils in the set of N coils, we find that there are $4N$ real scalar parameters necessary to describe the fields at each location, of which we can find $4N - 2$. The only additional knowledge required is the magnitude and phase of a single coil's negatively polarized field. Thus, although there is insufficient information available to calculate $\mathscr{F}$ directly, the amount of computation necessary to do so is expected to be reduced by approximately a factor of N compared to Direct RFIM reconstruction. The system's degrees of freedom are sufficiently reduced that its noise characteristics are expected to be comparable to those of fully linear RFIM.

2.1.2 Field Mapping Experiment

The field mapping procedure described in Section 2.1.1 was executed on a phantom in a 1.5T General Electric MRI. Values were taken by a simple gradient-echo pulse sequence, transmitting with the body coil (Coil a) and receiving with both the body coil and the elements of a head coil array (Coil b). The scans were made with cubic voxels of size $(2.8\text{mm})^3$. All scans were taken using $TR = 1000$ ms, and only the body coil was capable of transmit. The pulse length τ was chosen to make a (nominally) 45° pulse.

One slice through the scans is shown in Figure 2-1, from the body coil and one element of the head array. Notably, the phases 2.1.2 and 2.1.2 are identical up to measurement noise, exactly as predicted by Equation (2.8).
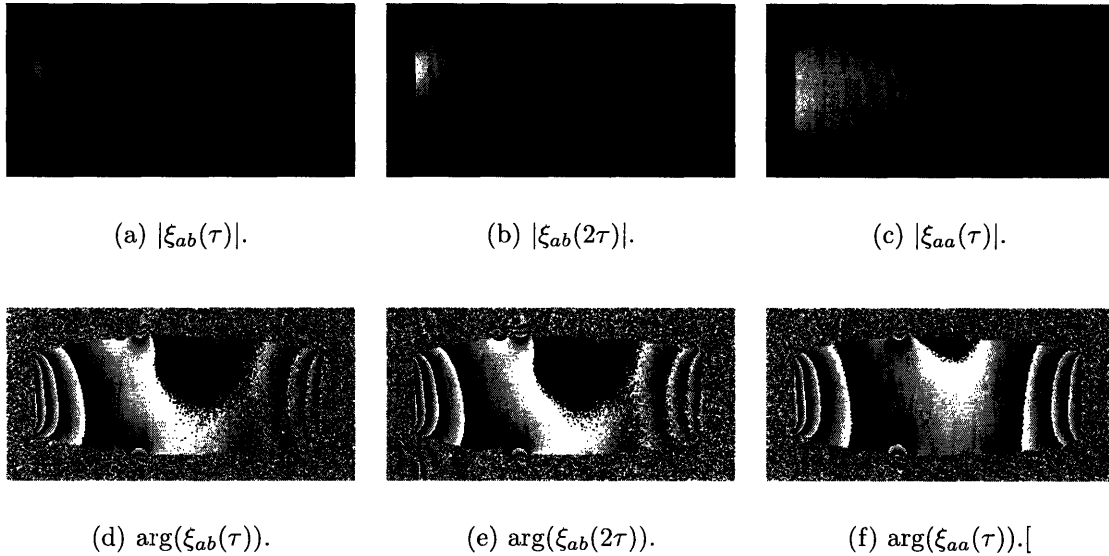

(a) $|\xi_{ab}(\tau)|$. (b) $|\xi_{ab}(2\tau)|$. (c) $|\xi_{aa}(\tau)|$.

(d) $\arg(\xi_{ab}(\tau))$. (e) $\arg(\xi_{ab}(2\tau))$. (f) $\arg(\xi_{aa}(\tau))$.[

Figure 2-1: Phantom scans in preparation for field mapping

Four independent properties of the B_1 fields are available: $\left|\mathscr{B}^+_{\text{body}}\right|$, $\left|\mathscr{B}^-_{\text{head}}/\mathscr{B}^-_{\text{body}}\right|$, $\arg\left(\mathscr{B}^+_{\text{body}}\right) - \arg\left(\mathscr{B}^-_{\text{head}}\right)$, and $\arg\left(\mathscr{B}^-_{\text{body}}\right) - \arg\left(\mathscr{B}^-_{\text{head}}\right)$. Maps of these properties are shown in Figure 2-2.

Figure 2.1.2 displays the difference between the phases of the two coils' receive fields. It is much more uniform than the other phase images. This appears to be due to the cancellation of the phase introduced by B_0 inhomogeneity. We may therefore conclude that the other phases are dominated by B_0 inhomogeneity, and that any experimental implementation of these protocols will require a B_0 map to cancel this artificial phasing.

2.1.3   Voxelization

In any real digital measurement, it is necessary to discretize the continuum. The continuous variable in this case is $\vec{x}$, and it is discretized by introducing a voxel matrix V. In a discretization with l voxels, V is a ∞-by-l real matrix whose l columns are

(a) $\left|\widetilde{\mathscr{B}}_a^+\right|$.

(b) $\left|\widetilde{\mathscr{B}}_b^- / \widetilde{\mathscr{B}}_a^-\right|$.

(c) $\arg\left(\widetilde{\mathscr{B}}_a^+\right) - \arg\left(\widetilde{\mathscr{B}}_b^-\right)$.

(d) $\arg\left(\widetilde{\mathscr{B}}_a^-\right) - \arg\left(\widetilde{\mathscr{B}}_b^-\right)$.
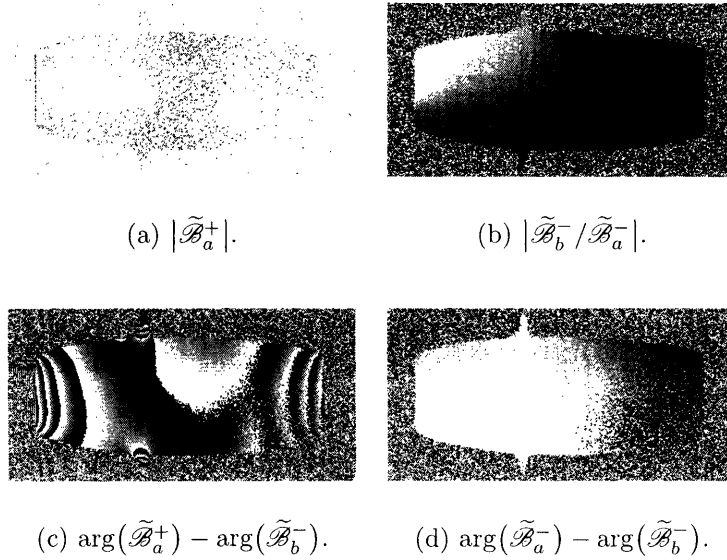
Figure 2-2: Field properties extracted directly from data in Figure 2-1

the voxels: orthonormal distributions over the patient volume. One obvious choice for V is l adjacent nonoverlapping cubes, forming a grid voxelization, but the voxels need not have any regular spatial pattern.

To approximate ς we introduce s, a length-l column vector such that $Vs \approx \varsigma$. Because the columns of V are orthonormal, the best approximation of ς is achieved by choosing $s = V^\dagger \varsigma$. By this definition s is the projection of ς onto the basis set described by V. We may then rewrite Equation (2.4) as

$$Z = \mathscr{F}\left(Vs + (\varsigma - Vs)\right). \tag{2.16}$$

The term $\varsigma - Vs$ is the component of the original image that is orthogonal to all of the voxels. We use the following definitions:

$$t \equiv |\varsigma - Vs| \, ; \tag{2.17}$$

$$U \equiv \frac{\varsigma - Vs}{t}. \tag{2.18}$$

U is a normalized column vector, like any column of V, and t is its magnitude, like a

23

single element of s. We may rewrite Equation (2.4) in more symmetrical form

$$Z = \mathscr{F}(Vs + Ut). \tag{2.19}$$

2.1.4 Error

RFIM is fraught with sources of error. Analysis of errors in Direct RFIM is intractable due to the complex behavior of iterative solvers in intermediate stages. As shown above, MRI is not sufficient to measure all of the components of the B_1 fields, so some iterated simulation is necessary. Nonetheless, an error analysis of Linear RFIM places an upper bound on the fidelity of more realistic RFIM approaches. There are two main sources of error in Linear RFIM: voxelization error and measurement noise. To distinguish exact and measured values, $\overline{x}$ will represent a measurement whose correct value is x, with error $\Delta x \equiv \overline{x} - x$. In this notation, the Linear RFIM reconstruction satisfies

$$\overline{Z} = \overline{\mathscr{F}}V\overline{s}. \tag{2.20}$$

There are two measurements that contribute to the Linear RFIM reconstruction: the impedances and the field map. Rewriting Equation 2.19 in terms of measured values and errors,

$$\overline{Z} - \Delta Z = \left(\overline{\mathscr{F}} - \Delta\mathscr{F}\right)\left(V\left(\overline{s} - \Delta s\right) + Ut\right). \tag{2.21}$$

The value of $\overline{s}$ is determined from $\overline{Z}$ by introducing a new matrix G such that $G\overline{\mathscr{F}}V = I$. G is a reconstruction matrix, and for sufficiently many coils ($N^2 > l$) there are infinitely many choices for G. The fundamental equation of linear reconstruction is

$$\overline{s} = G\overline{Z}. \tag{2.22}$$

24

To calculate the error in the final image, we note that

$$\Delta s = G\overline{Z} - s \tag{2.23}$$

$$= G\left(\Delta Z + \left(\overline{\mathscr{F}} - \Delta\mathscr{F}\right)\left(V\left(\overline{s} - \Delta s\right) + Ut\right)\right) - s \tag{2.24}$$

$$= G\left(\Delta Z - \Delta\mathscr{F}Vs + \mathscr{F}Ut\right). \tag{2.25}$$

If we make the simplifying Linear RFIM assumption that the field maps are highly accurate, i.e. $\Delta\mathscr{F} = 0$, then

$$\Delta s = G\left(\Delta Z + \mathscr{F}Ut\right). \tag{2.26}$$

Consider the case where there is also no error in the measurement of impedance, i.e. $\Delta Z = \Delta\mathscr{F} = 0$. If the body is completely representable by the voxels of V, then $Vs = \varsigma$ and $t = 0$. In this case, a noise-free reconstruction can exactly reproduce the correct map of ς. The $t = 0$ case is conceptually equivalent to taking a digital photograph of a perfectly aligned mosaic. If $t \neq 0$ then we will in general have $\overline{s} \neq s$. Specifically,

$$\Delta s = G\mathscr{F}Ut. \tag{2.27}$$

In RFIM, the component of the image orthogonal to the chosen voxels still contaminates their measured values. This error only disappears when $G\mathscr{F}U = 0$.

2.2 Image Segmentation

The voxel matrix V has been mentioned previously. In most imaging systems the voxelization is considered a detail. It is simply taken to be a square lattice, with a voxel profile specified as a point spread function. In RFIM, the relatively small number of measurements available (bounded above by N^2) limits the number of independent voxels. If the number of voxels exceeds N^2 then the system is underdetermined, and there are infinitely many possible images that satisfy the measurements.

In cases where there is no prior information available about the body being imaged,

the best choice of voxels may be a lattice of cubes. Consider a case where 128 coils are used to image a cubic volume. These coils provide approximately 8000 independent measurements, so the resolution of the resulting image can be no higher than $20 \times 20 \times 20$. In practice, the smoothness of the fields is expected to reduce the amount of information available, so the achievable resolution is likely to be even lower. This low resolution may be acceptable in many situations, but we would ideally like to increase the resolution. Any higher resolution reconstructions will be underdetermined.

One approach to solving underdetermined (and overdetermined) systems is Tikhonov Regularization. In Tikhonov Regularization, one adds an additional constraint: the solution must minimize some penalty function. For an image $I(\vec{x})$, one commonly chosen penalty is

$$m(I) = \int \left| \vec{\nabla} I \right|^2 d^3\vec{x}. \tag{2.28}$$

Minimizing $m(I)$ will generate the smoothest image that is consistent with the measurements.

For medical imaging, smooth images are not particularly desirable. The most useful medical imaging systems produce images with very sharp edges at the boundaries between different tissues. It is possible to construct a regularization that encourages this behavior. Suppose that an MRI image $P(\vec{x})$ is acquired along with the RFIM data. Then a penalty that encourages edges to fall in the right places is

$$m_e(I) = \int \frac{\left(\vec{\nabla} I \cdot \vec{\nabla} P\right)^2 + \alpha \left|\vec{\nabla} I \times \vec{\nabla} P\right|^2}{\left|\vec{\nabla} P\right|^4} d^3\vec{x}. \tag{2.29}$$

m_e is an ellipsoidal penalty based on the variations in P. Like $m(I)$, it penalizes all gradients in I, but it does so with weighting based on the gradient in P. Regions with a great deal of variation in the MRI image are also likely to have a great deal of variation in the RFIM image, so the penalty for variation there is lowered. Similarly, smooth regions in the MRI image are more likely to be smooth in the RFIM image.

If $\alpha > 1$ then the penalty for variation increases in the direction perpendicular to the gradient in P. One might visualize an ellipsoid of acceptable variation at each point with aspect ratio α and major axis $\vec{\nabla}P$. For $\alpha = 1$, this m_e simplifies to the spherical penalty

$$m_s(I) = \int \frac{\left|\vec{\nabla}I\right|^2}{\left|\vec{\nabla}P\right|^2} d^3\vec{x}. \tag{2.30}$$

In practice, Tikhonov Regularization is computationally expensive. The particular difficulty lies with the current approach to Direct RFIM, which uses an optimizer on the voxel values to reconstruct the image. The computational complexity of this optimization is superlinear in the number of voxels. Thus, increasing the number of voxels far beyond the number of measurements is infeasible.

In the hope of gaining many of the benefits of regularization with reduced computational requirements, we may take a less rigorous approach. Instead of applying the regularization throughout the reconstruction, we may apply it at the beginning by choosing a highly regular basis set. If the image is also highly regular, then this process should not greatly increase the penalty on the reconstructed image.

To choose the basis set, an analogy from quantum mechanics is helpful. Suppose we regard the penalty function as an energy, the Hamiltonian of a system whose state is the image. Given a low-energy state of the system, we expect from perturbation theory that it may be represented as a linear combination of low-energy eigenstates. To find the l lowest-energy eigenstates, we may use an iterative procedure. First, the procedure locates the ground state. In each subsequent step, it determines the lowest energy state that is orthogonal to all previously chosen states.

The basis set produced by this procedure can be used as the voxel matrix V for RFIM reconstruction. These voxels are very much unlike traditional voxels, as they overlap, and each one is nonzero over most of the volume. The analogy is also imperfect, as the penalty function is unlikely to be linear. Nonetheless, the procedure does generate a basis set that places edges in the same places as in the MRI prior.

Traditional image segmentation algorithms are also suitable for producing voxels

for the reconstruction.

2.3 Direct Map Extraction

It might seem intuitively that the field map, $\mathscr{F}$, need not be measured, and can simply be determined from the coil geometry by simulation. This is not the case, because the conductivity and permittivity distributions of the body affect the fields. The field map will be different for every scan, so it must be acquired anew each time.

This variability seems to imply that there is information available in the field. The question is how much information, and whether it can be medically useful. This question is best answered experimentally, but a theoretical analysis is required first.

As previously, we consider a system with the same permeability as free space, harmonic time variation at angular frequency ω, and linear conductivity. Maxwell's Equations are therefore

$$\vec{\nabla} \times \vec{\mathscr{E}} = -i\omega\vec{\mathscr{B}}; \tag{2.31}$$

$$\vec{\nabla} \times \vec{\mathscr{B}} = \mu_0(\sigma + \epsilon i\omega)\vec{\mathscr{E}}. \tag{2.32}$$

Since the MRI-based field mapping techniques more nearly map the magnetic fields than the electric fields, it seems sensible to combine these equations to express σ and ϵ in terms of $\vec{\mathscr{B}}$:

$$\vec{\nabla} \times \left(\frac{\vec{\nabla} \times \vec{\mathscr{B}}}{\mu_0(\sigma + \epsilon i\omega)} \right) = -i\omega\vec{\mathscr{B}}. \tag{2.33}$$

Applying vector identities and $\vec{\nabla} \cdot \vec{\mathscr{B}} = 0$,

$$\frac{1}{\mu_0(\sigma + \epsilon i\omega)}\nabla^2\vec{\mathscr{B}} + \left(\vec{\nabla} \times \vec{\mathscr{B}}\right) \times \vec{\nabla}\left(\frac{1}{\mu_0(\sigma + \epsilon i\omega)}\right) = i\omega\vec{\mathscr{B}}. \tag{2.34}$$

For ease of notation in discussing Equation (2.34), we introduce a variable P that encapsulates the electrical properties of the body at each location:

$$P := \frac{1}{\mu_0(\sigma + i\omega\epsilon)}. \tag{2.35}$$

28

Then we may transform Equation (2.34) to obtain

$$P\nabla^2\vec{\mathscr{B}} + \left(\vec{\nabla} \times \vec{\mathscr{B}}\right) \times \vec{\nabla}P = i\omega\vec{\mathscr{B}}. \qquad (2.36)$$

Given complete information about $\vec{\mathscr{B}}$, there exists a unique P that satisfies Equation (2.36).

Our goal is to determine the electrical property map, i.e., the value of P at each location. In principal, the condition imposed by Equation (2.36) is sufficient to produce such a map. We may simply consider every possible property map, checking to see if each one satisfies Equation (2.36). If we discretize the problem on a finite grid of points and set some tolerance for numerical errors, then such a search might even complete in finite time. In practice, it is not feasible to do an exhaustive search over the possible distributions of properties. Such a search would take years, conservatively, to produce a single property map. Thus, we require a feasible algorithm for computing a property map from $\vec{\mathscr{B}}$.

2.3.1 Iterative Reconstruction

In typical clinical applications, we expect that often P is nearly piecewise constant. Therefore, it may be sufficient to assume $\vec{\nabla}P \approx 0$ in many areas of the sample. In areas where this approximation is exact, Equation (2.36) becomes

$$P\nabla^2\vec{\mathscr{B}} = i\omega\vec{\mathscr{B}}. \qquad (2.37)$$

It is trivial to determine P from this equation, and the results in simulation confirm its correctness when $\vec{\nabla}P = 0$. However, when $\vec{\nabla}P$ is large, such as at boundaries between tissues, the results are incorrect by orders of magnitude.

One suggested exact algorithm attempts to improve this approximation by iteration. This iteration has not been proved to converge, and current implementations yield divergent results. Mathematically, it remains possible that the divergence is merely due to an implementation detail.

The iterative reconstruction starts with $P_0 = 0$, and generates each subsequent P_i using the recurrence relation

$$P_{i+1}\nabla^2\vec{\mathscr{B}} + \left(\vec{\nabla}\times\vec{\mathscr{B}}\right)\times\vec{\nabla}P_i = i\omega\vec{\mathscr{B}}. \qquad (2.38)$$

With this recurrence, P_1 is a solution to Equation (2.37). If the sequence converges, then P_∞ is a solution to Equation (2.36). In practice, this sequence does not appear to converge.

2.3.2 Variational Reconstruction

The variational reconstruction algorithm is based on the calculus of variations. In this approach, we calculate the difference between the right and left sides of Equation (2.36) at each location. The gradient of this error with respect to P may be determined by the Euler–Lagrange equations, and taking small steps down the gradient should reduce the error until a local minimum is found. This approach is expected to converge for sufficiently small step size, but current implementations diverge instead. The observed divergence may be caused by a software bug, or by the approximation of derivatives on a discrete lattice.

In our formulation, the Euler–Langrange equations contain both three-dimensional position vectors and abstract vectors and matrices. To reduce confusion, position vectors are labeled by a vector arrow (e.g., $\vec{x}$), and abstract vectors are printed in boldface (e.g., $\mathbf{f}$). The Euler–Lagrange equations can describe the behavior of a vector-valued function $\mathbf{f}(\vec{x})$ and a scalar-valued "action" functional $L(\mathbf{f},\mathbf{Df},\vec{x})$. The second argument, $\mathbf{Df}$, is a matrix containing the gradient of each component of $\mathbf{f}(\vec{x})$. In this formulation, the Euler–Lagrange Equations state that the functional gradient of L with respect to $\mathbf{f}$ is given by

$$(\nabla\mathbf{L})^i = \frac{\partial L}{\partial f^i} - \sum_{\mu=1}^{n}\frac{\partial}{\partial x^\mu}\frac{\partial L}{\partial f^i_\mu} \qquad (2.39)$$

where $f^i_\mu := \frac{\partial f^i}{\partial x^\mu}$, superscripts are indices, and $\vec{x}$ has $n = 3$ components.

In the case of property-map reconstruction, the variable function is the complex-valued scalar function $P(\vec{x})$. We may analyze P by defining f^1 as the real part of P and f^2 as the imaginary part. It quickly becomes apparent that the gradient of L with respect to P is given by

$$\nabla_P L = \left(\frac{\partial L}{\partial f^1} + i \frac{\partial L}{\partial f^2} \right) - \sum_{\mu=1}^{3} \frac{\partial}{\partial x^\mu} \left(\frac{\partial L}{\partial f^1_\mu} + i \frac{\partial L}{\partial f^2_\mu} \right). \tag{2.40}$$

To make L represent the error in Equation (2.36), we first introduce $\vec{Q}$, defined by

$$\vec{Q}(P) := P \nabla^2 \vec{\mathscr{B}} + \left(\vec{\nabla} \times \vec{\mathscr{B}} \right) \times \vec{\nabla} P - i\omega \vec{\mathscr{B}}. \tag{2.41}$$

Under this definition, $\vec{Q}$ is a complex vector functional of P with the property that Equation (2.36) is equivalent to $\vec{Q} = 0$. Finding the function P that most nearly satisfies Equation (2.36) is equivalent to minimizing the magnitude of $\vec{Q}$. This equivalence allows us to use the Euler–Lagrange method. To apply the Euler–Lagrange method to this minimization we choose $L := \vec{Q} \cdot \vec{Q}^*$.

Computing all of the functional derivatives is a relatively straightforward matter of algebra, and the result is most easily written as follows:

$$\vec{C} := \vec{\nabla} \times \vec{\mathscr{B}}, \tag{2.42}$$

$$\nabla_P L = 2 \vec{Q} \cdot \nabla^2 \vec{\mathscr{B}}^*$$

$$- \left(\frac{\partial}{\partial x} \left(2\vec{Q} \cdot \begin{bmatrix} 0 \\ c^z \\ -c^y \end{bmatrix} \right) + \frac{\partial}{\partial y} \left(2\vec{Q} \cdot \begin{bmatrix} -c^z \\ 0 \\ c^x \end{bmatrix} \right) + \frac{\partial}{\partial z} \left(2\vec{Q} \cdot \begin{bmatrix} c^y \\ -c^x \\ 0 \end{bmatrix} \right) \right). \tag{2.43}$$

To minimize L, it should be sufficient to use simple Euler integration on this first-order differential equation. Specifically, by using a recurrence of the form

$$P_{i+1} = P_i - \alpha \nabla_P L, \tag{2.44}$$

31

it should be possible to reach a local minimum of L for a sufficiently small positive step size α.

Current implementations of this algorithm do not converge. This matter is a topic of current investigation.

2.3.3   Explicit Formulation

In Section 2.3, we considered the problem of reconstructing the electrical properties of a body from a complete map of the magnetic field. Both the iterative and the variational reconstructions rely on complete knowledge the magnetic fields of the coils. As noted in Section 2.1.1, complete knowledge of the fields is not actually available. Therefore, the approaches described in Sections 2.3–2.3.2 are insufficient to treat the problem at hand. In this section, we determine whether the available knowledge about the fields is theoretically sufficient to determine the electrical properties of the body. To do so, we formulate explicitly the system of equations relating the measured field attributes to the desired electrical properties. This formulation does not require complete information about the magnetic fields of the coils.

For simplicity, we consider the case of two coils, labeled a and b. As shown in Section 2.1.1, a system with two coils has six different independent measurable quantities related to the magnetic fields of the coils. In this section, we show that these six quantities are sufficient to uniquely determine the electrical properties of the body.

To distinguish between quantities that are known from measurement and quantities that are to be determined by the system of equations, measured quantities are set off in square brackets. All other quantities are unknown complex scalar functions of position, including P, which represents the electrical properties that we seek to map.

As stated in Section 2.1.1, in order to complete our description of the fields, we require two additional real variables, or a single complex variable. There are many possible choices for this additional variable. For this derivation, that additional complex variable has been chosen for convenience to be $\widetilde{\mathscr{B}}_a^-$. From this circularly

polarized field component, we may introduce equations to reconstruct the other three:

$$\widetilde{\mathscr{B}}_a^+ = \left[|\widetilde{\mathscr{B}}_a^+|\right] u\!\left(\widetilde{\mathscr{B}}_a^-\right) \left[\frac{u\!\left(\widetilde{\mathscr{B}}_a^+\right)}{u\!\left(\widetilde{\mathscr{B}}_a^-\right)}\right] ; \tag{2.45}$$

$$\widetilde{\mathscr{B}}_b^+ = \left[|\widetilde{\mathscr{B}}_b^+|\right] u\!\left(\widetilde{\mathscr{B}}_a^-\right) \left[\frac{u\!\left(\widetilde{\mathscr{B}}_b^+\right)}{u\!\left(\widetilde{\mathscr{B}}_a^-\right)}\right] ; \tag{2.46}$$

$$\widetilde{\mathscr{B}}_b^- = \widetilde{\mathscr{B}}_a^- \left[\frac{|\widetilde{\mathscr{B}}_b^-|}{|\widetilde{\mathscr{B}}_a^-|}\right] \left[\frac{u\!\left(\widetilde{\mathscr{B}}_a^+\right)}{u\!\left(\widetilde{\mathscr{B}}_a^-\right)}\right] \left[\frac{u\!\left(\widetilde{\mathscr{B}}_a^+\right)}{u\!\left(\widetilde{\mathscr{B}}_b^-\right)}\right]^{-1} . \tag{2.47}$$

We may relate the circular components to the corresponding Cartesian components by reversing Equations (2.5) and (2.6), introducing four more equations into the system:

$$\mathscr{B}_{ax} = \widetilde{\mathscr{B}}_a^+ + \widetilde{\mathscr{B}}_a^{-*}; \tag{2.48}$$

$$\mathscr{B}_{ay} = -i \cdot \left(\widetilde{\mathscr{B}}_a^+ - \widetilde{\mathscr{B}}_a^{-*}\right) ; \tag{2.49}$$

$$\mathscr{B}_{bx} = \widetilde{\mathscr{B}}_b^+ + \widetilde{\mathscr{B}}_b^{-*}; \tag{2.50}$$

$$\mathscr{B}_{by} = -i \cdot \left(\widetilde{\mathscr{B}}_b^+ - \widetilde{\mathscr{B}}_b^{-*}\right) . \tag{2.51}$$

The divergence of a magnetic field is always zero, so we may introduce two more equations into the system to provide the z-component of both magnetic fields:

$$\frac{\partial}{\partial x}\mathscr{B}_{ax} + \frac{\partial}{\partial y}\mathscr{B}_{ay} + \frac{\partial}{\partial z}\mathscr{B}_{az} = 0; \tag{2.52}$$

$$\frac{\partial}{\partial x}\mathscr{B}_{bx} + \frac{\partial}{\partial y}\mathscr{B}_{by} + \frac{\partial}{\partial z}\mathscr{B}_{bz} = 0. \tag{2.53}$$

From the complete Cartesian components of the fields, we may now expand Equation (2.36). The z-component of that vector equation is redundant in this formulation because the $\mathscr{B}_{az}$ and $\mathscr{B}_{bz}$ were computed from the x- and y- components. Therefore, we write only the x- and y-components of Equation (2.36):

$$P\nabla^2 \mathscr{B}_{ax} + \left(\frac{\partial}{\partial z}\mathscr{B}_{ax} - \frac{\partial}{\partial x}\mathscr{B}_{az}\right)\frac{\partial P}{\partial z} - \left(\frac{\partial}{\partial z}\mathscr{B}_{ay} - \frac{\partial}{\partial y}\mathscr{B}_{ax}\right)\frac{\partial P}{\partial y} = i\omega\mathscr{B}_{ax}; \tag{2.54}$$

$$PV^2\mathscr{B}_{ay} + \left(\frac{\partial}{\partial x}\mathscr{B}_{ay} - \frac{\partial}{\partial y}\mathscr{B}_{ax}\right)\frac{\partial P}{\partial x} - \left(\frac{\partial}{\partial y}\mathscr{B}_{az} - \frac{\partial}{\partial z}\mathscr{B}_{ay}\right)\frac{\partial P}{\partial z} = i\omega\mathscr{B}_{ay}; \quad (2.55)$$

$$PV^2\mathscr{B}_{bx} + \left(\frac{\partial}{\partial z}\mathscr{B}_{bx} - \frac{\partial}{\partial x}\mathscr{B}_{bz}\right)\frac{\partial P}{\partial z} - \left(\frac{\partial}{\partial z}\mathscr{B}_{by} - \frac{\partial}{\partial y}\mathscr{B}_{bx}\right)\frac{\partial P}{\partial y} = i\omega\mathscr{B}_{bx}; \quad (2.56)$$

$$PV^2\mathscr{B}_{by} + \left(\frac{\partial}{\partial x}\mathscr{B}_{by} - \frac{\partial}{\partial y}\mathscr{B}_{bx}\right)\frac{\partial P}{\partial x} - \left(\frac{\partial}{\partial y}\mathscr{B}_{bz} - \frac{\partial}{\partial z}\mathscr{B}_{by}\right)\frac{\partial P}{\partial z} = i\omega\mathscr{B}_{by}. \quad (2.57)$$

There are thirteen independent relations in this system, most of which are trivial transformations between different bases. In total, the dependent variables in these equations are the four circularly polarized components, the six cartesian components, and P. There are eleven dependent variables and thirteen distinct relations among them. Therefore, for two coils, the system is overdetermined. Because the system is determined, it must be possible to solve for the values of all the variables, including P, the variable of interest.

This statement of determinacy generalizes easily to systems with more than two coils. A system with many coils may be regarded as a two-coil system by disregarding all but two of the coils. Therefore, all systems with at least two coils are completely determined. A closer analysis shows that the degree of overdeterminacy increases rapidly as the number of coils increases.

Finding a solution to this system of equations is regarded as significantly more challenging than finding a solution to Equation (2.36) given full knowledge of $\vec{\mathscr{B}}$. Given that no method has yet been found to solve Equation (2.36), a great deal of ingenuity is expected to be required to solve this system of thirteen equations. In fact, an ideal method of solution would not only solve the entire system, but would find the approximate solution with minimum error if no exact solution exists due to measurement error.

2.4 Data Fusion Impedance Mapping

Both the impedance of MRI coils and MRI images themselves provide data about the underlying permittivities and conductivities. Combining the data from both methods should provide improved images. A simultaneous reconstruction might use

34

the impedance data to stabilize the low spatial frequencies and the MRI data to image local details.

Chapter 3

Applications

3.1 New Imaging Modalities

Different tissues in the body have significantly different values of ϵ and σ at radio frequencies. Thus, RFIM could provide images of anatomy. The effects of most pathologies on permittivity and conductivity have not yet been examined, but embolisms, edema, and other pathologies that affect the geometry of the body should be recognizable in an RFIM image [6].

The key question for diagnostic imaging is image quality. The technology will be effective for clinicians only if it provides sufficient detail and clarity to distinguish diagnostic features. It is not yet clear whether the RFIM techniques discussed here will have sufficiently high resolution and SNR to be of clinical use.

3.2 Improving Existing Imaging Modalities

3.2.1 SAR Mapping

In MRI, the greatest danger to the safety of patients (after proper screening for metal objects) is tissue heating. This heating is produced by the absorption of radiation. In recognition of the danger posed by radiation heating, it is subject to the US federal guidelines on Specific Absorption of Radiation, or *SAR*. These guidelines specify

maximum allowed power deposition densities. All medical MRI machines are designed with these guidelines in mind, but they do not attempt to determine the exact induced SAR distribution.

In order to determine SAR, it is necessary to know the fields of the coils and the conductivity map of the body. Given these two parameters one may calculate the SAR from the strength of the transmitting B_1 field. Specifically, at each location the power density ρ is given by

$$\rho = \left\langle \sigma \left| \vec{E} \right|^2 \right\rangle \tag{3.1}$$

Exact mapping of SAR has not been seen as crucial in current clinical MRI equipment, but at higher fields it is seen as a major problem [7]. The amount of heating grows with the square of the field strength, so the potential for injury to the patient is greater in stronger fields. The SAR pattern depends on the electrical properties of the patient's body, and the strength of this dependence increases with field strength as well, reducing the effectiveness of one-size-fits-all models. Finally, the spatial frequencies in the SAR map increase with field strength, providing further amplification of SAR beyond square-law in small regions. Thus, a complete map of the B_1 fields may be critical for ensuring patient safety in future MRI machines.

3.2.2   Coil Sensitivity Modulation

The advanced field mapping techniques described here may prove necessary in high-field MRI machines. Normally, MRI images are reconstructed under the assumption that the magnitude of some large coil's field is uniform. This assumption is explicit in parallel imaging, but it is also implicit in non-accelerated MRI. The assumption yields a good approximation at low Larmor frequencies, but as the field strength increases to 3T and beyond, this assumption breaks down and artifacts appear.

Electrical property mapping provides a potential solution to this problem. If the fields can be quantified at each location, then the images produced by the scanner may be normalized to remove artifacts. Since the magnitude of the fields is likely to be smooth compared to anatomical details, this application is less demanding of

resolution than diagnostic imaging.

Chapter 4

Conclusion

The family of RFIM techniques contains three classes of modalities: Direct RFIM, MRI-Assisted RFIM, and Map Extraction. All of these techniques have hardware requirements very similar to the newest generation of parallel imaging MRI scanners. The major remaining barriers to implementation are theoretical and algorithmic. For Direct RFIM, an algorithm exists for reconstruction, but it is very slow and probably produces suboptimal results. For MRI-Assisted RFIM, no algorithm has successfully recovered the unknown receive field. Finally, for Direct Map Extraction, no algorithm has demonstrated correct reconstruction of electrical properties from fields.

This situation may sound unfortunate, but there is reason for optimism. The problem has not yet been analyzed by researchers whose focus is on numerical algorithms. Moreover, current approximate solutions may prove clinically useful, even if they are not theoretically defensible. The final goal of this research is unequivocally clinical, and on that front things are looking up.

Bibliography

[1] Grant, Aaron. *Radio Frequeny Impedance Mapping for Medical Imaging.* NIH Grant 5R21EB003306-03. 1 July 2003.

[2] Grant, Aaron and Daniel Sodickson. "Dielectric Imaging Using Resonant RF Circuits". Unpublished. January 2004.

[3] Private communications with Aaron Grant and Daniel Sodickson, Summer 2005–January 2006.

[4] Haacke, E. Mark et. al. "Magnetic Resonance Imaging: Physical Principles and Sequence Design," Wiley-Liss, 1999.

[5] Hoult, D. I. *The principle of reciprocity in signal strength calculations - A mathematical guide,* Concepts Magn. Reson. **12** (2000), 173–187.

[6] H. Scharfetter, R. Casañas, and J. Rosell. "Biological Characterization by magnetic induction spectroscopy." *IEEE Trans. Biomed. Eng.* vol. 50, pp. 870–880, 2003.

[7] Hu, Xiaoping, and David G. Norris. "Advances in High-Field Magnetic Resonance Imaging." Annu. Rev. Biomed. Eng. 2004., pp. 157–184.